Constraints on Ground Deformation Processes at the Tulu Moye Volcanic Complex, Main Ethiopian Rift

Birhan Abera Kebede[a,c], Carolina Pagli[a], Freysteinn Sigmundsson[b], Derek Keir[c,d] Alessandro La Rosa[a], Snorri Gudbrandsson[e]

[a] Department of Earth Sciences, University of Pisa; [b] School of Engeneering and Natural Sciences, University of Iceland; [c] Department of Earth Sciences, University of Florence; [d] School of Ocean and Earth Science, University of Southampton, e Rekjavik Geothermal

Abstract

Tulu Moye is an actively deforming volcanic complex with a geothermal field in the Main Ethiopian Rift. We use InSAR between 2014 and 2022, integrated with other geophysical data, to investigate the temporal and spatial characteristics of the deformation signal in the area, and to model its source. Velocity maps and time-series analysis show a deformation signal consistent with uplift at a velocity of up to 50 mm/yr in the satellite line-of-sight (LOS) in 2014-2017, then decreasing to 12 mm/yr until 2022. The centre of deformation is located about 10 km west of a main geothermal drilling site at Tulu Moye, between the Bora, Berecha, and Tulu Moye volcanoes, with a NW-SE elongation direction. Our best-fit model suggests that the deformation is caused by an 8.7 km by 1.2 km sill situated ~7.7 km below the surface (~5.9 km below sea-level), elongate in the N54°W direction and dipping S11°W, and experienced an average velocity of volume change of ~8.9×10^6 m^3/yr in 2014-2017. The surface projection of the sill overlaps with local transverse faults and hydrothermal manifestations. The sill is ~1-2 km below clusters of microseismic swarms and a region of high resistivity, both indicating hydrothermal fluid flow. The location and geometry of the sill correlates with the upper edge of high conductivity interpreted as a zone of partial melt, and we therefore attribute the uplift at the Tulu Moye volcanic complex to inflow of magma in the sill. We also suggest that the transverse caldera rims faults may restrict magma flow, and also facilitate both vertical and lateral hydrothermal fluid flow.

1. Introduction

Volcanoes with a geothermal field are complex systems where the migration and accumulation of a variety of fluid phases (magma, hydrothermal fluids and gases) can potentially contribute to the surface deformation. Geodetic techniques, such as Interferometric Synthetic Aperture Radar (InSAR), have revealed spatial and temporal characteristics of volcano deformation in great detail and have improved our understanding of the underlying plumbing systems (e.g., Lundgren et al., 2020; Albino and Biggs, 2021; Bato et al., 2021; Sigmundsson et al., 2022). However, determining the type of fluid involved from a deformation source from geodetic data alone is difficult, since multiple fluid types can act as a pressurised source. Therefore, independent subsurface constraints are useful to help interpret deformation sources. For example, Gottsmann et al. (2020) used microgravimetry data at Corbetti (Ethiopia) to determine that magma influx rather than hydrothermal fluids was most likely responsible for observed uplift detected in that area using InSAR. An additional information can be taken from the Gudjónsdóttir et al. (2020), who studied the Krýsuvík geothermal system (Iceland) and showed that periods of GPS detected crustal deformation were associated with elevated seismicity and elevated gas emissions, thereby

interpreting that the deformation was caused by migration of the hydrothermal fluids through fractures. Chiodini et al. (2015) studied an inflation period during 2014 in Campi Flegrei caldera (Italy) by comparing long term record of fumarolic compositions to ground deformation. The authors concluded that the gas plume in the hydrothermal system was the cause of inflation.

The Main Ethiopian Rift (MER) is an area of magma-rich continental rifting that is at the northern end of the East African rift system. The MER links to the southern Red Sea Rift and western Gulf of Aden via the Afar depression, where the Nubian, Somalian and Arabian plates form a rift-rift-rift triple junction (Figure 1A; e.g., Chorowicz, 2005; Corti, 2009; Tortelli et al., 2022). The MER has nearly 60 active volcanoes (Aspinall et al., 2011), many of which have vigorous hydrothermal systems fuelled by magmatic heat sources, and some that are deforming (e.g., Haledebi, Fentale, Kone, Aluto, Corbetti and Tulu Moye) (Albino et al., 2022). The hydrothermal systems of the MER host geothermal energy resources that have the potential to produce a significant amount of electricity (> 10,000 MW) from about 23 geothermal sites that have been identified (e.g., UNDP, 1973; Kebede, 2016). Analysis of ground deformation at deforming volcanoes provides the opportunity to model the source of the deformation, and when interpreted with other geological and geophysical data allows to better understand the source of ground deformation and the relationship between the magmatic and hydrothermal systems. In this paper we integrate InSAR, magnetotelluric (MT) and seismic data to investigate the magmatic system that drives the geothermal field at the Tulu Moye volcanic complex in the MER.

1.1 Geology and tectonic setting

The MER started to form at ~6-10 Ma with extension thought to have been initially accommodated by the NE striking border faults (e.g., Woldegabriel et al., 1990; Wolfenden et al., 2004; Abebe et al., 2010). Extension has become more localised through time within the rift valley, and during the last 2 Myrs is thought to have been focused to ~20 km-wide, ~70 km-long magmatic segments that strike NNE and are arranged in a right stepping, en-echelon fashion in the rift (Ebinger and Casey, 2001; Siegburg et al., 2020). The magmatic segments have volcanic centres such as the Tulu Moye volcanic complex, aligned cone fields, and lava flows. They are cut by the NNE striking Wonji Fault Belt (WFB) which is made of small-offset normal faults and fissures (Boccaletti et al., 1998). The MER also has ~NW to WNW-striking faults roughly transverse to the rift (Korme et al., 2004; Corti et al., 2009). The origin of these faults is debated, with alternative hypotheses proposed (e.g. Benvenuti et al., 2023). They may relate to reactivation of across-rift faults in the Precambrian basement formed during pre-Cenozoic mountain building and rifting events (Korme et al., 2004; Stern et al., 1990), presence of caldera faults (e.g. Casey et al., 2006; Acocella et al., 2002), and/or regional faults formed during Cenozoic Gulf of Aden/Red Sea rifting (Abebe et al., 1998).

The Tulu Moye volcanic complex is of Quaternary age and and lies within the central sector of the MER. It is about 80 km from the capital city of Ethiopia, Addis Ababa (Figure 1A). It is surrounded by the rift Lake Ziway to the south, and Lake Koka and Gedemsa caldera to the north. The Tulu Moye volcanic complex consists of different volcanic edifices (Bora, Oda, Berecha, Werdi, Giano, and Tulu Moye) and calderas (Figure 1B). It is characterised by young volcanism, faulting and a hydrothermal activity. Late Pleistocene-Holocene pyroclastic deposits, basaltic and silicic lava flows and domes are dominantly erupted from the main silicic edifices of Bora, Berecha, and Tulu Moye, as well as from Oda and Werdi edifices (Figure 1B; Di Paola, 1972; Abebe et al., 2005; Tadesse et al., 2022). The youngest fissure eruptions of silicic domes and scoria cinder cones are situated along the NNE-striking Salen range (Varet and Birba, 2018), where the main focus of

geothermal activity and drilling occurs (Figure 1B). The most recently erupted silicic dome from the Salen range is the Giano dome (Figure 1B), dated as 1900 CE (Gouin, 1979; Wadge et al., 2016). The volcanic rocks are intensely cut by both west and east dipping WFB faults, but also intersected by a population of the transverse faults (Figure 1B).

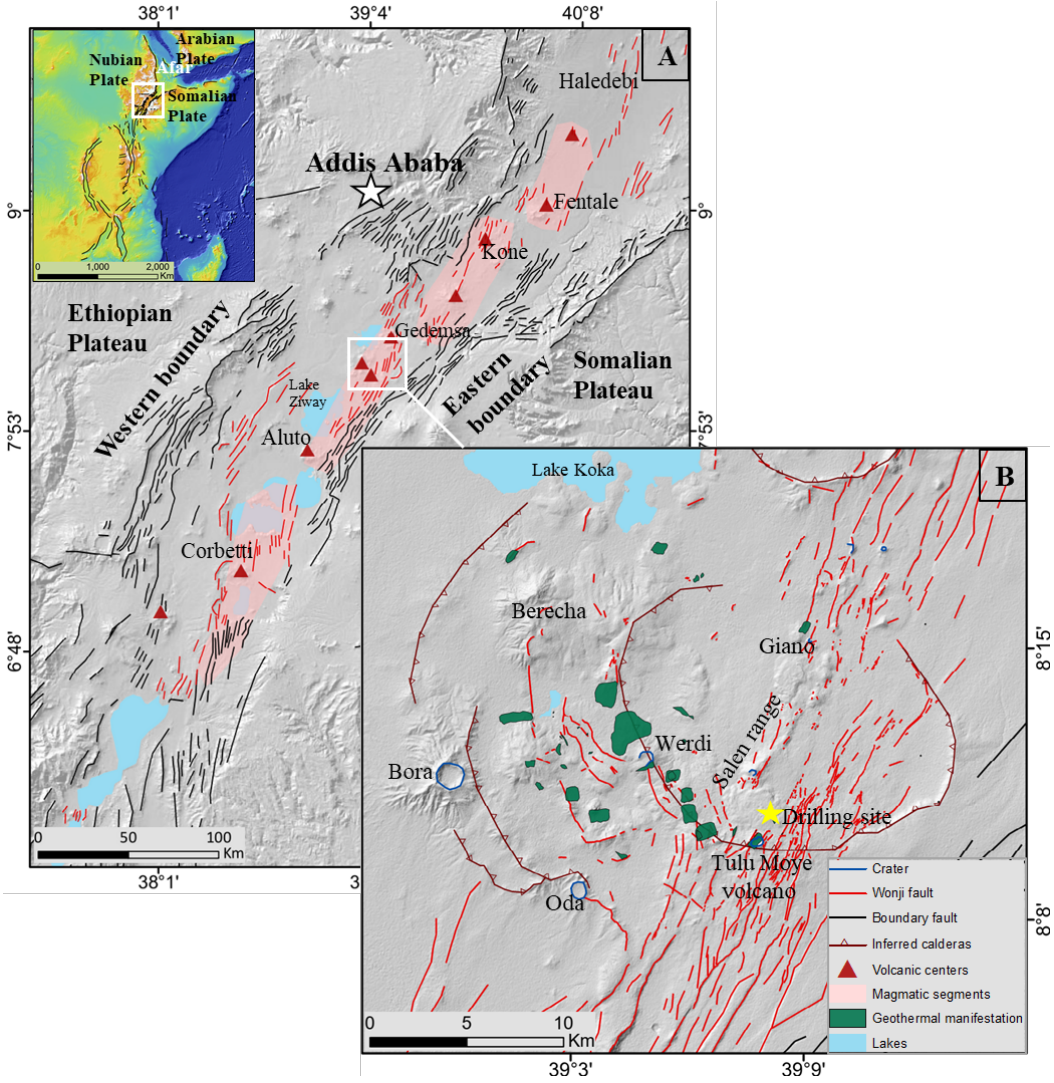

Figure 1. A) Tectonic map of the Main Ethiopian rift, based on Agostini et al. (2011a) with the inset map of the East African Rift System. B) Tectonic map of Tulu Moye volcanic complex, adapted from Abera (2021). The locations of surface geothermal manifestation are modified from Ayele et al. (2002).

The Tulu Moye volcanic complex includes evidence for caldera collapse events (Figure 1B; Gudbrandsson et. al., 2020; Abera, 2021), although the surface expression of the caldera collapse faults is debated (e.g., Korme, 1999; Varet & Birba, 2018; Gudbrandsson et. al., 2020). However, they can be broadly mapped based on the apparent remnants of the various caldera rims visible in satellite images (Gudbrandsson et. al., 2020; Abera, 2021). The innermost caldera is best defined and surrounds the Salen range (Figure 1B). It is elongated in a NW-SE direction, similar to most calderas in the MER (Acocella et al., 2002). The caldera is 17 km wide in the NW-SE direction and

11 km wide in the NE-SW direction, and it is intensely cut by the WFB (Figure 1B). The caldera collapse is dated to 107.7 ± 8.8 Ka, and it is the youngest caldera collapse event in the central MER (Tadesse et al., 2022). To the west and south-west of this caldera there are two inferred caldera structures that are not easily recognized at the surface, but rather can be traced from the satellite images following the patchy appearances of the caldera rim remnants (Figure 1B). South-west of the Salen range, there is the shortest caldera rim remnant. It extends from the foot of Mount Bora to the Oda crater, and dips NE toward the innermost caldera. The outermost caldera extends from the Oda crater, passes through Bora, and terminates near Lake Koka. This caldera rim bounds the western side of the Tulu Moye volcanic complex. In addition, the transverse faults occur between the caldera rims and follow the circular shape of the rims, suggesting that the origin of the transverse faults in Tulu Moye is related to the formation of the calderas (Figure 1B).

Hydrothermal processes at the Tulu Moye volcanic complex are intense and expressed at the surface in the form of fumaroles, steaming, and altered grounds. These surface manifestations are mainly in the western part of the complex, along the transverse faults and near Tulu Moye volcano (Figure 1B). Currently, geothermal exploration activities are in progress in the area by a private company, Tulu Moye Geothermal Operations plc (TMGO), aiming to generate electricity. MT surveying has revealed electrically conductive bodies at various depths (Samrock et al., 2018; Gudbrandsson et. al., 2020). The shallowest is in the upper ~2 km beneath most of the Tulu Moye volcanic complex and interpreted as a shallow clay cap. Below this, a more localised conductive body is imaged at ~4 km depth beneath Tulu Moye volcano and is interpreted as a magma reservoir and the heat source for the geothermal system (Samrock et al., 2018; Gudbrandsson et. al., 2020). Below, a south-west dipping conductive anomaly extends from 4 to 20 km depth, and is interpreted as related to a series of stacked bodies of partial melt (Samrock et al., 2018). A highly resistive body is also identified west of Tulu Moye volcano at about 2-4 km depth, and interpreted as related to the presence of hot hydrothermal fluids and associated rock alteration (Samrock et al., 2018). This location also corresponds to clusters of shallow (2-5 km-deep) microseismicity, interpreted to be triggered by the migration of the hydrothermal fluids (Greenfield et al., 2019a, b; Figure 6).

On a regional scale, InSAR observations along the whole MER have identified deformation signals on several active volcanoes, including Haledebi, Fentale, Kone, Aluto, Corbetti and Tulu Moye (Figure 1A; e.g., Biggs et al., 2011; Hutchison et al., 2016; Lloyd et al., 2018; Temtime et al., 2018; Albino and Biggs, 2021). Other than the Haledebi volcanic area where deformation is likely caused by faulting, either episodic magmatic inflows or hydrothermal activity, or both were inferred as causes of the observed deformation. Biggs et al. (2011) used ENVISAT InSAR data to show that the Tulu Moye volcanic complex experienced two pulses of uplift in 2004 and 2008-2010 with intervening subsidence. These observations were modelled in terms of a 2.5 km deep penny shaped crack and interpreted as a magmatic heat source that drives hydrothermal activity and inflation. The uplift during 2008-2010 occurred at a velocity of about 2 cm/yr and although it was not formally modelled, it was interpreted as the result of inflation in the hydrothermal system, with fluids migrating along permeable paths of transverse faults and caldera rim (Samrock et al., 2018). An increased (3 cm/yr) uplift velocity was also observed between 2015 and 2020 using Sentinel-1 data (Albino and Biggs 2021), but in this case, it was not modelled and instead broadly interpreted to be caused by magmatic pressurization in the caldera system.

Tulu Moye is an actively deforming volcanic area in the MER, with the deformation source attributed in the past literature to being both a magmatic source or related to hydrothermal activity. There remains debate regarding the locus, shape and origin of the deformation. In this study, we

invert InSAR observations during 2014-2017 and integrate our best-fit model with results from magnetotelluric methods and seismicity to explore the nature and geometry of the deformation source, and investigate the magmatic plumbing system of the Tulu Moye volcanic complex.

2. Data Analysis and results

2.1 InSAR data Analysis

We used InSAR data acquired by the European Space Agency (ESA) Sentinel-1A and 1B satellites during 2014-2022. Data from the two satellites in both ascending (track 087) and descending (track 079) geometries were acquired for 2014-2017, with data for only the descending geometry available through to 2022. The interferogram processing and subsequent time-series analysis was performed on the ESA's Geohazards Exploitation Platform (GEP), using the P-SBAS (Parallel Small BAseline Subset) Interferometry module (Casu et al., 2014; De Luca et al., 2015) to derive cumulative deformation time-series and average velocity maps in the satellite Line-of-Sight (LOS) (Figure 2). For the interferogram generation, the topographic phase contributions were removed using the Shuttle Radar Topography Mission (SRTM) DEM) with a 1-arcsec pixel size (e.g., Farr et al., 2007)). A Goldstein power spectrum filter of 0.5 was also used to filter the interferograms (Goldstein and Werner, 1998). Our interferograms have perpendicular baselines ranging between 1-145 m and temporal baselines between 24-264 days for the descending track (079), and perpendicular baseline of 15-168 m and a temporal baseline range of 24-385 days for the ascending track (Appendix A. Supplementary Material, Fig. S1).

The P-SBAS technique includes two main atmospheric noise filtering components. The noise component due to atmospheric stratification, which is highly correlated with topography but weakly in time, is first removed from the unfiltered time series (Fernández et al., 2009). Then, the noise component characterized by a high spatial correlation but a low temporal correlation is identified and filtered with APS (Atmospheric Phase Screening) while the pixels that exhibit time-progressive deformation (highly correlated temporally) are left unchanged (De Luca et al., 2022). The phase unwrapping was performed by using Extended Minimum Cost Flow (EMCF) algorithm (Pepe and Lanari, 2006; Manunta et al., 2019).

For the 10/2014 - 03/2017 period a total of 197 interferograms were processed, with 94 and 103 interferograms from ascending and descending, respectively. For the 03/2017-10/2022 an additional 417 interferograms were calculated from the descending geometry only, as ascending acquisition ended in 2017.

2.1.1 Deformation patterns and Time series

A clear deformation signal is evident in both ascending and descending InSAR velocity maps, covering an area of ~100 km^2, between the Bora, Berecha, and Tulu Moye volcanic edifices (during 2014-2017) (Figure 2A, B). The signal in both tracks is characterized by a concentric pattern, elongated NW-SE and centred in an area to the west of the geothermal drilling site at Tulu Moye volcano. Both the descending and ascending velocity maps show LOS range decrease, consistent with a dominant uplift of the ground component, at a velocity reaching up to 50 mm/yr. To better visualize the spatial pattern of deformation, we made two profiles across the centre of the deformation signals (Figure 2C, D), parallel and orthogonal to the NW-SE elongation direction.

Profiles of both orbits show the highest values (~40-50 mm/yr) at the centre, gradually reducing away from it.

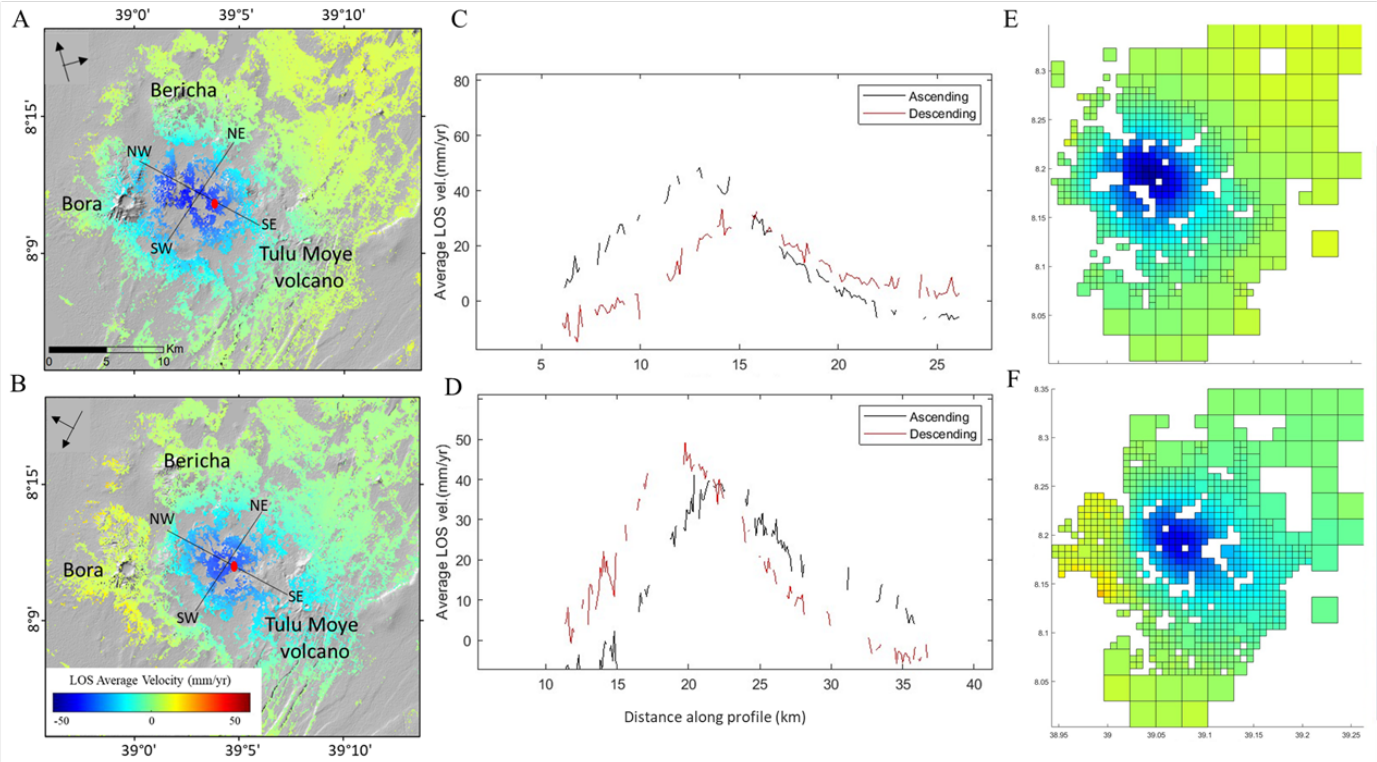

Figure 2. A) LOS velocity maps for ascending track 087 and B) descending track 079 during 2014-2017. C) Profiles across the ascending and descending velocity maps along the NE-SW and (D) along the NW-SE direction. E) Quad-tree partitioning of the ascending and F) descending tracks. The red dot in figure A and B represents the point where data for the time-series analysis was taken in figure 3.

The time series of cumulative LOS displacements for 2014-2017 in ascending and descending tracks show a consistent time-evolving deformation pattern with deformation starting in mid-2015 with a rapid LOS velocity of about 50 mm/yr until 2017 (Figure 3). For the 2017-2022 time-period only descending data are available showing that the uplift velocity slowed and decayed until the end of 2018. From 2019 onwards, the LOS change has continued at an approximately linear velocity of ~12 mm/yr until 2022. The overall pattern shows some fluctuations with short periods of small-scale uplift and subsidence that is sometimes rapid (Figure 3).

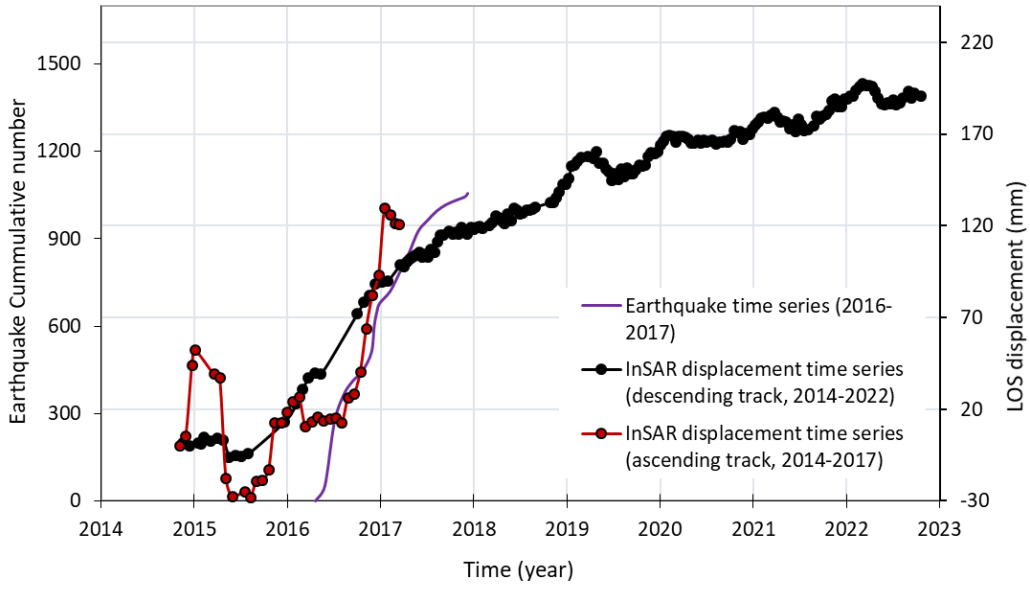

Figure 3). Time series of cumulative LOS displacements of a point in the centre of the uplift from the descending (blacl) and ascending (red) tracks and cumulative number of earthquakes (blue) during 2016-2017 modified from Greenfield et al. (2019). The x-axis ticks mark the start of each year in January.

2.2 Modelling

To quantify the parameters of the deformation source beneath the Tulu Moye volcanic complex we jointly inverted the ascending and descending InSAR velocity maps, assuming a uniform rectangular dislocation sill model, (Okada, 1985) in a homogeneous, isotropic, elastic half-space with a Poisson's ratio of 0.25. We chose the sill model to match the observed NW-SE elongated deformation pattern that would not be reproduced by symmetric sources (e.g. Mogi). We jointly inverted the velocity maps (Figure 4) to find the best fitting source parameters of the sill using a Monte-Carlo simulated annealing algorithm and then a derivative (quasi-Newton) based method (Cervelli et al., 2001; Wang et al., 2014). Before the inversion, the interferograms were quad-tree partitioned (Figure 2E, F) in order to reduce the data size (e.g., Jonson et al., 2002; Wang et al., 2014), assuming a maximum standard deviation threshold of 2 mm for both the ascending and descending velocity maps.

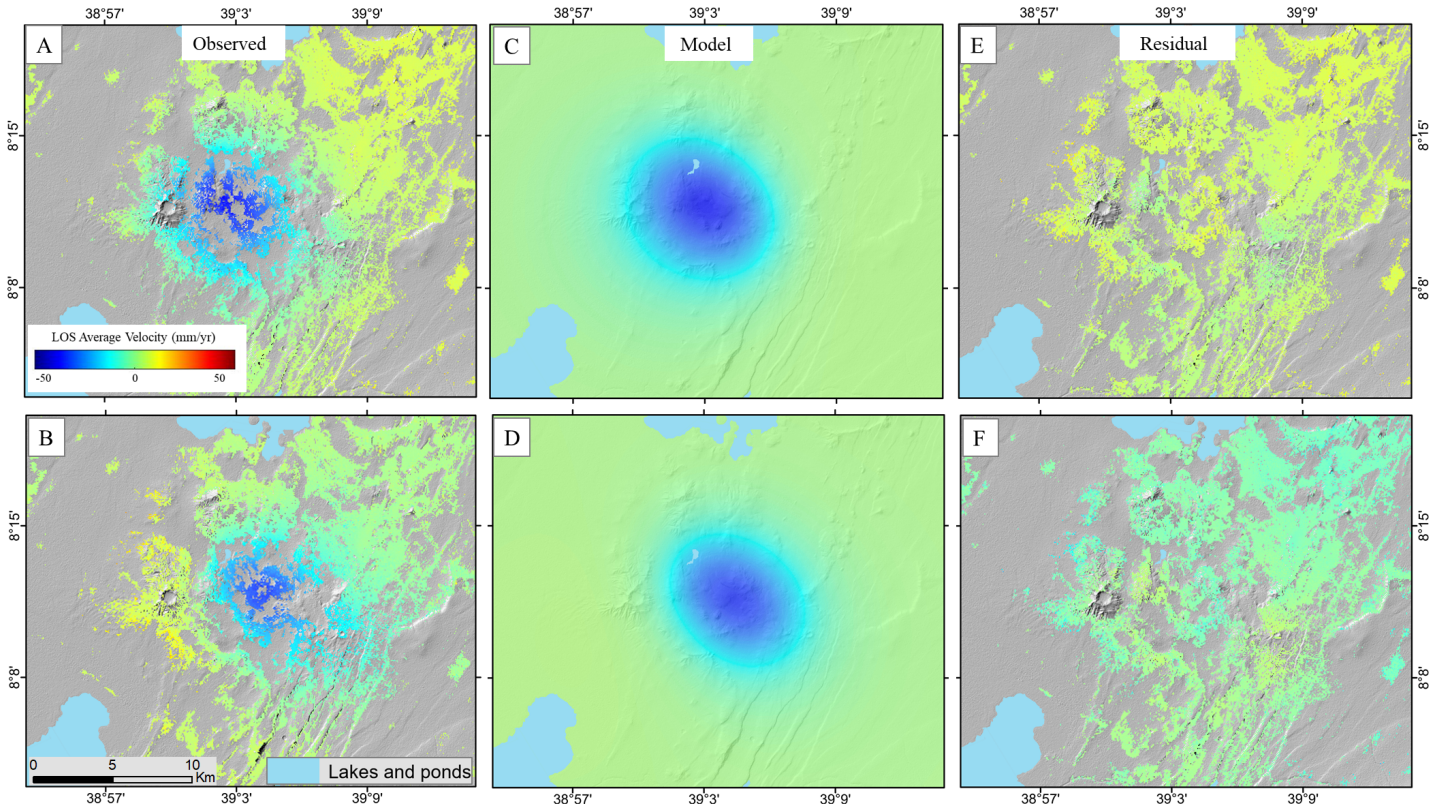

Figure 4. Observed velocity maps in ascending (A) and descending (B) paths, predicted LOS change for best-fit horizontal sill model in ascending (C) and descending (D) paths, and residuals between observed and best-fit model LOS changes in ascending (E) and descending (F) paths.

Furthermore, a Monte Carlo simulation of correlated noise was used to estimate the uncertainties on the source parameters (e.g., Wang et al., 2014; Wright et al., 2003). This is performed by creating 100 simulations of spatially correlated random noise based on the variance-covariance matrices of each velocity map. The simulations are added to the observed data and inverted to get 100 model solutions. The uncertainty of each parameter is estimated from the statistical distribution of the 100 solutions and the 90% confidence interval of each model parameter was calculated (Table 1).

We find that a sill elongated N54°W at 7.7 km depth below the surface best match our data. The sill is 8.7 km long and 1.2 km wide with an opening of 0.8 m/yr corresponding to a volume change of 8.9×10^6 m^3/yr. We initially fixed the sill to be horizontal but in a second approach, we allowed the sill to dip. Overall, both best-fit models are similar and have a comparable RMS misfit (2.4, 2.8 and 2.4, 2.7 mm/yr for ascending and descending tracks for the horizontal and dipping sill models, respectively). The best-fit dipping model has a dip of 11° towards the south-west, but the other model parameters show insignificant changes whether we assume the sill is horizontal or dipping.

Source parameters	Depth (km)	Length (km)	width (km)	Opening (m/yr)	Strike (°)	Dip (°)	Longitude (°)	Latitude (°)	Calculated Volume (m^3/yr)
Values	7.7	8.7	1.2	0.83	54 NW	0	39.0619	8.187	$8.7x10^6$
90% CI	7.4 - 8	7.9 - 9.7	1.2 - 1.5	0.65 - 0.86	59 - 48 NW	0	39.061 - 39.064	8.186 - 8.189	$8 x10^6$- $9 x10^6$
Values	7.7	8.7	1.2	0.85	55 NW	11 SW	39.066	8.194	$8.9x10^6$
90% CI	7.3 - 8.1	7.9 - 9.6	1 - 1.6	0.66 - 0.89	60 - 50 NW	17 - 6 SW	39.064 - 39.068	8.190 - 8.197	$8x10^6$- $9.6x10^6$

Table 1. Best-fit sill model parameters with their 90% confidence interval (CI). The best-fit values in the upper two rows are for the horizontal sill model and the lower two rows are for the dipping sill model.

Figure 5 shows the inferred distribution of pairs of, and individual, model parameters. Source parameters that show trade-off with other parameters are less well constrained compared to parameters that do not trade-off. We observe negative correlation between width and opening (Figure 5A), indicating that a wider sill trades off with less opening. We also calculated the sill volume and observe a positive correlation of volume with depth (Figure 5A). Thus, model sources at different depths and experiencing different volume changes generate similar LOS patterns on the surface, and more specifically that deeper sill models require larger amount of volume change. Allowing the sill to dip introduces additional trade-offs between dip and latitude, and between dip and longitude (Figure 5B), indicating that the sill location is less well-constrained compared to solutions assuming a horizontal sill. A trade-off is also observed between width and length implying that majority of the wider sources trade off with a shorter sill and vice versa (Figure 5B).

A

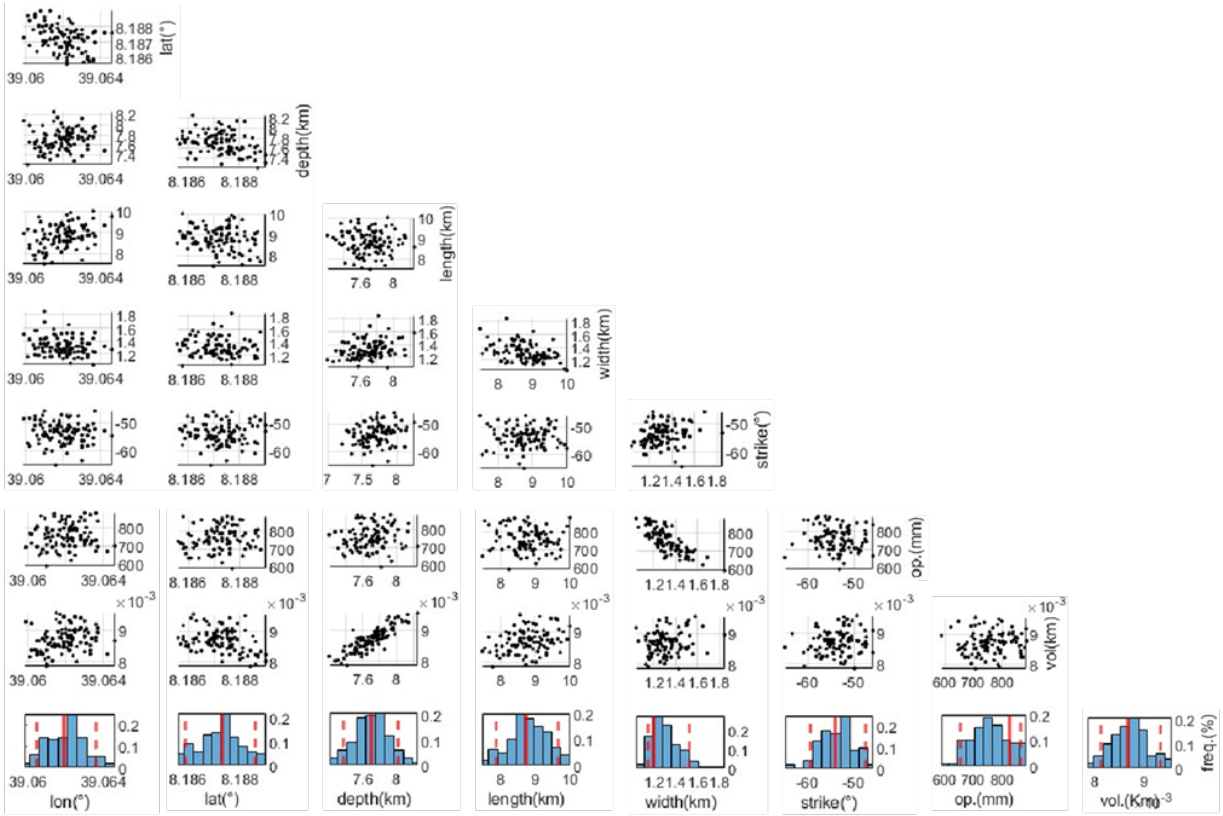
lat(°)
depth(km)
length(km)
width(km)
strike(°)
op.(mm)
vol(km)
freq.(%)
lon(°)
lat(°)
depth(km)
length(km)
width(km)
strike(°)
op.(mm)
vol.(Km)

B

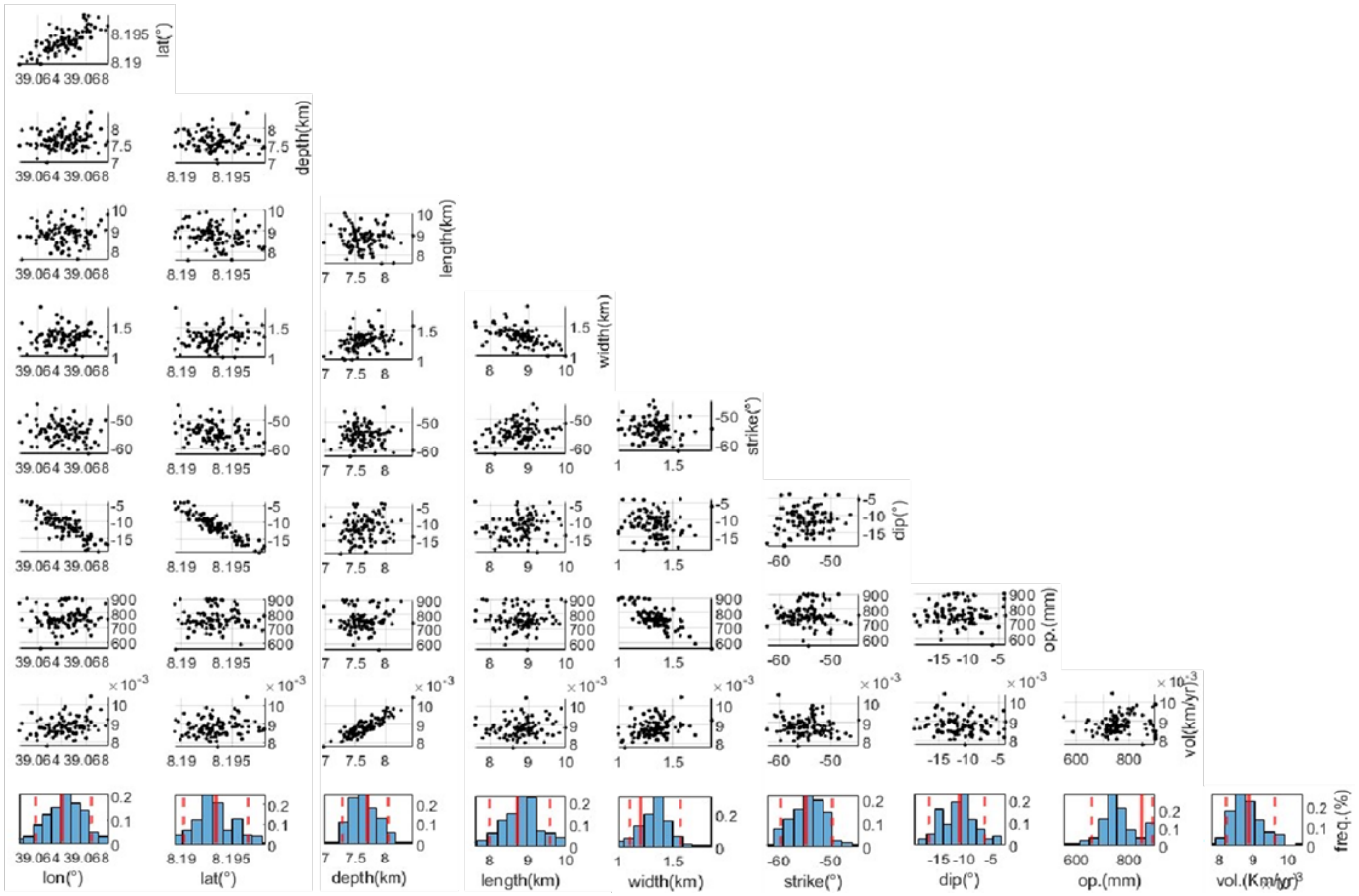
lat(°)
depth(km)
length(km)
width(km)
strike(°)
dip(°)
op.(mm)
freq.(%)
lon(°)
lat(°)
depth(km)
length(km)
width(km)
strike(°)
dip(°)
op.(mm)

Figure 5. Scatter plots and histograms of individual and pairs of model parameters for the sill fixed to be horizontal (A) and the dipping sill (B). The solid red line in the histograms represent the best-fit solution for the given parameter. The red vertical dashed lines delimit the 90% confidence intervals.

3. Discussion

3.1 Deformation source

Our model for the 2014-2017 InSAR data reveals a deeper (7.7 km) inflating body that can be explained by a sill shape expanding at a velocity of volume increase of ~8.9×10^6 m^3/yr. The previous dedicated InSAR study at the Tulu Moye volcanic complex used data acquired from 2003 to 2010. The study showed inflation in 2004 and 2008-2010, which the authors modelled with a Penny-shaped crack and interpreted as being caused by hydrothermal activities at a depth shallower than 2.5 km (Biggs et al., 2011). The average uplift velocity during 2008-2010 was up to 20 mm/yr (Biggs et al., 2011; Samrock et al., 2018), lower than our observations of 50 mm/yr in 2014-2017. The fact that the majority of deformation is about 10 km west of the main active geothermal heat source near Tulu Moye volcano makes the understanding of the deformation source challenging. Our modelling indicates that an inflating sill is situated at a depth of 7.7 km below the surface, which is ~5.9 km depth Below Sea Level (BSL), and that it possibly dips towards the SW. This depth is ~1-2 km below the base of the cluster of microseismicity identified from a dense network of seismic stations during 2016-2017, with the spatial and temporal character of the seismicity indicative of them being triggered by hydrothermal fluid migration (Greenfield et al., 2019a; Figure 6B).

Interpretation of MT data (Samrock et al., 2018) has revealed a SW dipping conductive zone in the area of the modelled sill, interpreted as a region of partial melt with a series of stacked sills connecting a deep crustal melt reservoir to a ~4 km deep and localised magma reservoir (and assumed geothermal heat source) near Tulu Moye volcano to the east. Our modelled sill corresponds to the upper edge of the highly conductive zone in MT studies dipping to the SW (Samrock et al., 2018; 2021). Our best-fit dipping sill has a dip angle aligned to the top edge of the dipping conductive body. We therefore interpret the source of the deformation as being the inflow of magma into a sill shaped magma body. A magmatic origin to the deformation is supported by global observations in that hydrothermal systems rarely reach to 7 km depth, but instead more commonly localised in the uppermost ~3 km of the crust (e.g., Teng and Koike, 2007; Chambefort et al., 2016; Gola et al., 2017; Teklemariam et al., 1996; Helgadóttir et al., 2010).

The MT results show that above our modelled sill is a region of high resistivity and there is also microseismicity at ~2-5 km depth, both interpreted as indicative of the active hydrothermal system (Samrock et al., 2018; Greenfield et al., 2019a). Our results raise the possibility that the sill that we model from InSAR is an additional heat source that drives hydrothermal fluid circulation above it. The observed velocity of uplift is not constant but instead peaks during mid-2015 to 2017 and suggests that flow of magma into the sill shaped magma body is pulsed, and peaked during this time period (Figure 3). The pattern of uplift in the InSAR time series shares similarities to variations in rate of microseismicity, which peaks during 2016 but reduces in rate in early 2017 coincident with the reduction in uplift velocity (Figure 3). The correlation can be explained as the increase in magma flux into the sill thermally driving more vigorous hydrothermal circulation above it (e.g., Tolstoy et al., 2008), or from the increased velocity of crustal deformation stressing the faults in the

hydrothermal system to failure (e.g. Bell et al., 2021). Since 2018, the InSAR time series shows varying velocity of uplift followed by short periods of subsidence that may suggest episodic inflows in the system.

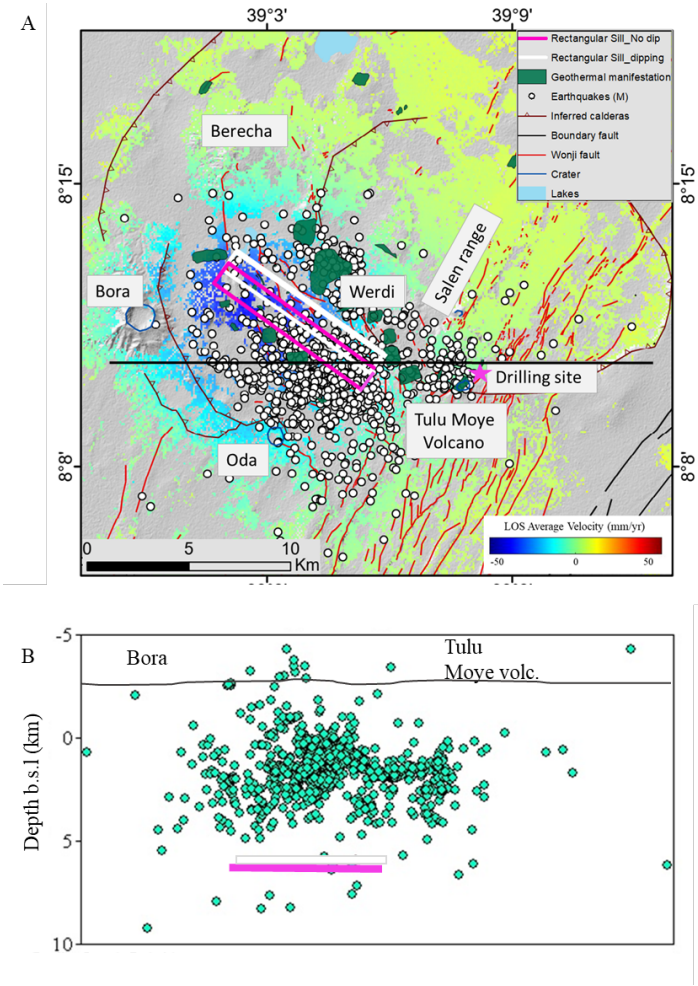

Figure 6. A) InSAR velocity map 2014-2017 in the ascending path, with tectonic structures, the surface hydrothermal manifestations, the inferred caldera rim, the earthquakes, and the surface projections of the horizontal (pink) and SW-dipping (white) modelled sills. The black horizontal line is the seismicity profile in part B. (B) our sill models, along with the hypocentral distribution of earthquakes from Greenfield et al. (2019a).

3.2 The link between magmatic and hydrothermal systems

The observed uplift and the modelled sill are located west of the NNE-oriented WFB, and instead lies beneath a caldera system of the Tulu Moye volcanic complex. The caldera system potentially exerts an important control on the magmatic ~~system~~ and overlying hydrothermal systems. Numerical models of the stress state beneath caldera topography shows that sill shaped magma intrusions are favoured beneath the caldera structure, with sub-vertical dikes instead favoured beneath and outside the caldera rims (Corbi et al., 2015), a model that partly explains the occurrence of our sill within the caldera system. In detail, our modelled sill is positioned below an area characterized by a series of NW-SE oriented faults, which appear to be part of a series of the remnant caldera rims. The modelled sill is locally sub-parallel to the nearby NW striking faults and placed between two concentric caldera rims (Figure 6A), corroborating the hypothesis that the orientation of the sill is fault controlled. More specifically the spatial association between the sill and NW striking faults

suggests the sides of the long axis of the sill are potential bound by faults. Studies from Thverfell magmatic complex of SW Iceland have shown evidence that the geometry of magma emplacement can be influenced by the existing tectonic structures (Pasquare and Tibaldi, 2007; Tibaldi et al., 2008). A batholith emplacement controlled by the structures in Andes, Peru is an additional example of fault controlled magma intrusion (Pitcher and Bussell, 1977). We therefore interpret that the NW oriented across rift faults likely act to channel and restrict flow of magma into an elongate sill shape that we interpret as being fed from the SW dipping zone of partial melt imaged in MT studies beneath the complex.

An additional observation is that the position and orientation of our modelled sill spatially correlates to the surface hydrothermal manifestations, which are mainly altered ground (clay deposits) and fumaroles that are aligned following the various inferred caldera related faults (Figure 6A). The spatial correlation is clearest in our dipping sill model in that the surface hydrothermal manifestations surround, within ~1-2 km distance, the edges of the sill. Such an observation suggests the NW-SE faults also provide a path for hydrothermal fluid flow above the sill. This interpretation would also imply further support that our modelled sill is the primary heat source in the western portion of the Tulu Moye volcanic complex. Alternatively, if our modelled sill is not driving hydrothermal circulation, the NW trending faults could act as westward migration pathways for hydrothermal fluids heated by the geothermal heat source located at a depth of 4 km near Tulu Moye volcano.

3.3 Comparison to other systems

The deformation signal observed in the Tulu Moye volcanic complex can be compared to other volcanic and hydrothermal systems of the MER as well as globally. The Aluto and Corbetti volcanic systems are active Quaternary calderas forming central volcanoes, situated south of the Tulu Moye volcanic complex within the central part of the MER (Figure 1A). Both are characterized by intense hydrothermal activity. Aluto is roughly 70 km south of Tulu Moye. Deformation at Aluto is episodic, which shows consistency with the seasonal precipitation and lake loading conditions (Albino and Biggs, 2021), and the signals are explained by a coupled magmatic-hydrothermal system (Biggs et al., 2011; Hutchison et al., 2016). Episodic magmatic intrusion cause inflation, while degassing of the hydrothermal system is responsible for subsidence. Before 2008, the depth of the deformation sources was found to be shallow (2.5 km; Biggs et al., 2011), while the depth of an inflation source between 2008 and 2010 was 5 km (Hutchison et al., 2016). The episodic behaviour and depth of the sources of deformation during 2008 makes the deformation at Aluto similar to the Tulu Moye volcanic complex.

The Corbetti volcanic complex, about 145 km south of Tulu Moye, has been observed from InSAR time series of different time periods showing uplift with an intervening subsidence (Biggs et al., 2011; Gottsmann et al., 2020; Albino, Lloyd et al., 2018). From interpretation of InSAR data and models along with MT and seismicity (Lloyd et al. 2018; Lavaysiere et al., 2019) hydrothermal fluid flow on both WFB and across rift faults was interpreted as being driven by deeper magmatic processes. Gottsmann et al. (2020) was more specific, and used the increase in absolute microgravity during observed uplift to model the source of deformation to be intrusion of mafic magma at ~7 km depth, similar to our study. Apart from their similarities in geology, tectonics, and geothermal systems, the deformation in Aluto and Corbetti can be compared with the Tulu Moye volcanic complex by its style, source, and source depth. Overall, it is evident that the shallow (< 7 km) upper

crustal melt and/or hydrothermal activity, which are commonly focused in the WFB, are the sources of deformation in the central sector of the MER.

Our InSAR study shows that observation and modelling of ground deformation at volcanoes can improve our understanding of subvolcanic and hydrothermal systems. Using multidisciplinary datasets we define a new model of the hydrothermal and magmatic system of Tulu Moye (Figure 7).

Conclusions

This study has revealed the source and geometry of the deformation signal observed by InSAR from Sentinel-1A/B during 2014-2017 in the Tulu Moye volcanic complex. The InSAR observation from the ascending (087) and descending (079) tracks has defined the presence of an elongated inflating body between Bora, Berecha and Tulu Moye volcanoes. Inverse modelling of the inflation signal solved the geometry and depth of the deformation source, signifying the presence of a sill shaped body at a depth of ~7.7 km below the surface (~5.9 km below sea level) slightly dipping to the SW. The sill depth is below the shallow zone of microseismicity and highly resistive hydrothermal alteration zone, but within a conductive partial melt zone inferred from magnetotelluric studies. We therefore interpret a magmatic origin to the deformation. The inferred inflating sill is below the surface trace of NW-trending faults, and surface hydrothermal manifestations, indicating the orientation of the modelled sill may be structurally controlled and potentially be an important heat source in the western part of the hydrothermal system.

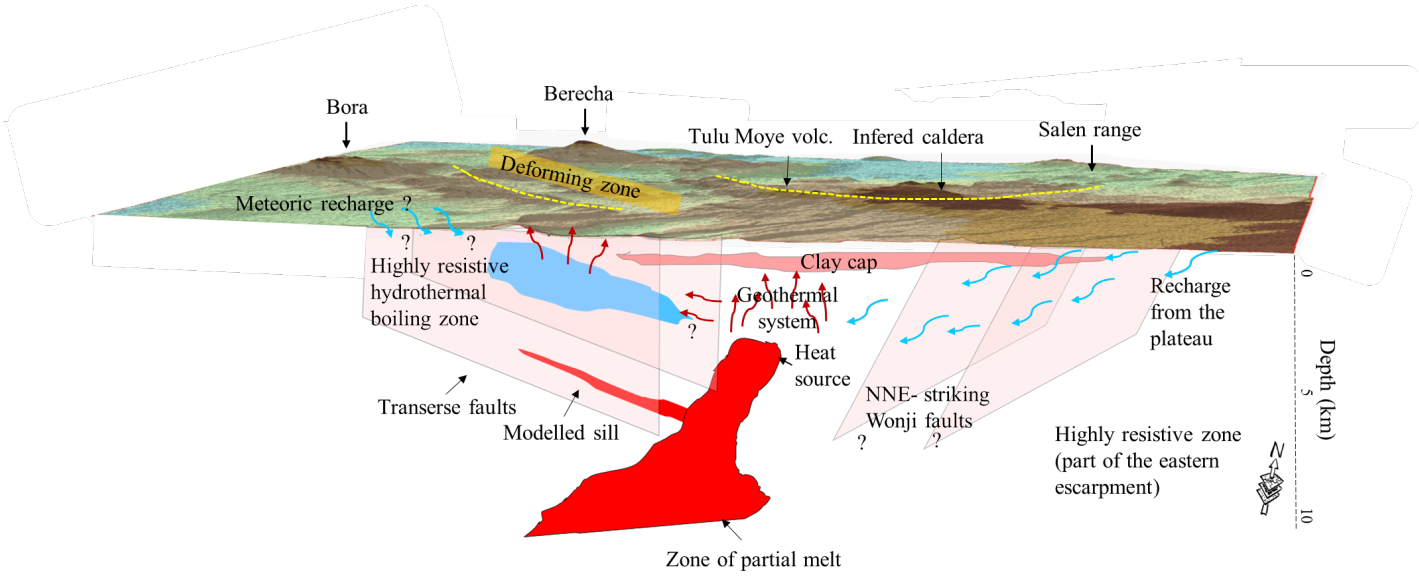

Figure 7. Schematic east-west cross-section for the Tulu Moye volcanic complex, demonstrating the locus of the modelled sill with respect to other elements of the magmatic, structural, and hydrothermal system. The zone of partial melt in red and the clay cap in pink are based on high conductivity zones from Samrock et al. (2018). The sill is a schematic view of our InSAR model. The hydrothermal boiling zone in blue is based on high resistivity zone from Samrock et al. (2018). The subsurface planes are interpreted faults.

Acknowledgements:

This work is part of PhD project under the XXXVII cycle of the Dottorato Regionale Pegaso in Earth Sciences; and supported by the Ministero Università e Ricerca (MiUR) with the National Operational Program (PON)-Action IV.5 “PhDs on green issues”. We would like to thank Reykjavik Geothermal plc. for allowing Birhan Abera Kebede to conduct her internship program. We acknowledge support by the ESA (European Space Agency) NoR (Network of Resources) initiative for Geohazards Exploitation Platform (G-TEP). We particularly thank Hervé Caumont and Michele Sica from Terradue for the support with G-TEP.

References

Abebe, T., Balestrieri, M.L. and Bigazzi, G., 2010. The central Main Ethiopian rift is younger than 8 Ma: Confirmation through apatite fission-track thermochronology. Terra Nova, 22(6), 470-476. https://doi:10.1111/j.1365-3121.2010.00968

Abebe, T., Manetti, P., Bonini, M., Corti, G., Innocenti, F., Mazzarini, F. and Pecskay, Z., 2005. Geological map (scale 1: 200,000) of the northern Main Ethiopian Rift and its implication for the volcano-tectonic evolution of the rift. Geol. Soc. Am. Map Chart Ser., MCH094.

Abebe, T., Mazzarini, F., Innocenti, F., & Manetti, P,1998. The Yerer-Tullu Wellel volcanotectonic lineament: A transtensional structure in central Ethiopia and the associated magmatic activity. Journal of African Earth Sciences, 26(1), 135-150.

Abera, B, 2021. The Relationship between the Tulu Moye Geothermal System, the Ziway–Asela Area and the Tectonic Structure of the Ethiopian Rift (Masters thesis).

Acocella, V. and Korme, T., 2002. Holocene extension direction along the main Ethiopian Rift, East Africa. Terra Nova, 14(3), 191-197. https://doi.org/10.1046/j.1365-3121.2002.00403.x

Acocella, V., Korme, T. and Salvini, F., 2002. Formation of normal faults along the axial zone of the Ethiopian Rift. Journal of Structural Geology, 25(4), 503-513. https://doi.org/10.1016/S0191-8141(02)00047-0

Agostini, A., Bonini, M., Corti, G., Sani, F. and Manetti, P., 2011a. Distribution of quaternary deformation in the central Main Ethiopian Rift, East Africa. Tectonics, 30(4). https://doi.org/10.1029/2010TC002833

Albino, F., & Biggs, J., 2021. Magmatic processes in the East African Rift System: Insights from a 2015–2020 Sentinel-1 InSAR survey. Geochemistry, Geophysics, Geosystems, 22, e2020GC009488. https://doi.org/10.1029/2020GC009488

Albino, F., Biggs, J., Lazecký, M. and Maghsoudi, Y., 2022. Routine Processing and Automatic Detection of Volcanic Ground Deformation Using Sentinel-1 InSAR Data: Insights from African Volcanoes. Remote Sensing, 14(22), e2020GC009488. doi.org/10.3390/rs14225703

Aspinall, W., Auker, M., Hincks, T., Mahony, S., Nadim, F., Pooley, J., Sparks, R.S.J. and Syre, E., 2011. Volcano hazard and exposure in GFDRR priority countries and risk mitigation measures. Volcano Risk Study, pp.0100806-00.

Ayele, A., Teklemariam, M., Kebede, S., 2002. Geothermal Exploration in the Abaya and Tulu Moye-Gedemsa Prospects, Main Ethiopian Rift. Geological Survey of Ethiopia, Addis Ababa. p. 79.

Bato, M.G., Lundgren, P., Pinel, V., Solidum Jr, R., Daag, A. and Cahulogan, M., 2021. The 2020 eruption and large lateral dike emplacement at Taal volcano, Philippines: Insights from satellite radar data. Geophysical Research Letters, 48(7), e2021GL092803. https://doi.org/10.1029/2021GL092803.

Bell, A.F., Hernandez, S., La Femina, P.C. and Ruiz, M.C., 2021. Uplift and seismicity driven by magmatic inflation at Sierra Negra Volcano, Galápagos Islands. Journal of Geophysical Research: Solid Earth, 126(7), e2021JB022244.

Benvenuti M., Corti G., Keir D. and Sani F, 2023. Transverse tectonics control on the Late Quaternary development of the Central Main Ethiopian Rift. Italian Journal of Geosciences, 142(1), 42-56, https://doi.org/10.3301/IJG.2023.05.

Biggs, J., Bastow, I., Keir, D., and Lewi, E., 2011. Pulses of deformation reveal frequently recurring shallow magmatic activity beneath the Main Ethiopian Rift. Geochemistry, Geophysics, Geosystems, 12, Q0AB10. https://doi.org/10.1029/2011GC003662

Boccaletti, M., Bonini, M., Mazzuoli, R., Abebe, B., Piccardi, L. and Tortorici, L., 1998. Quaternary oblique extensional tectonics in the Ethiopian Rift (Horn of Africa). Tectonophysics, 287(1-4), 97-116. https://doi.org/10.1016/S0040-1951(98)80063-2

Casey, M., Ebinger, C.J., Keir, D., Gloaguen, R., Mohamad, F., 2006. Strain accommodation in transitional rifts: extension by magma intrusion and faulting in Ethiopian rift magmatic segments. In: Yirgu, G., Ebinger, C.J., Maguire, P.K.H. (Eds.), The Afar Volcanic Province within the East African Rift System: Geological Society Special Publication, 259, 143–163.

Cervelli, P., M. H. Murray, P. Segall, Y. Aoki, and T. Kato, 2001. Estimating source parameters from deformation data, with an application to the March 1997 earthquake swarm off the Izu Peninsula, Japan, Journal of Geophysical Research, 106(B6), 11,217–11,237. https://doi:10.1029/2000JB900399

Chambefort, I., Buscarlet, E., Wallis, I.C., Sewell, S. and Wilmarth, M., 2016. Ngatamariki geothermal field, New Zealand: Geology, geophysics, chemistry and conceptual model. Geothermics, 59, 266-280. https://doi.org/10.1016/j.geothermics.2015.07.011

Chiodini, G., Vandemeulebrouck, J., Caliro, S., D'Auria, L., De Martino, P., Mangiacapra, A. and Petrillo, Z., 2015. Evidence of thermal-driven processes triggering the 2005–2014 unrest at Campi Flegrei caldera. Earth and Planetary Science Letters, 414, 58-67.

Chorowicz, J., 2005. The East African Rift System. Journal of African Earth Sciences, 43, 379-410. https://doi:10.1016/j.jafrearsci.2005.07.019

Corbi, F., Rivalta, E., Pinel, V., Maccaferri, F., Bagnardi, M. and Acocella, V., 2015. How caldera collapse shapes the shallow emplacement and transfer of magma in active volcanoes. Earth and Planetary Science Letters, 431, 287-293. https://doi.org/10.1016/j.epsl.2015.09.028

Corti, G., 2009. Continental rift evolution: from rift initiation to incipient break-up in the Main Ethiopian Rift, East Africa. Earth-Science Reviews, 96(1-2), 1-53. https://doi.org/10.1016/j.earscirev.2009.06.005

De Luca, C., Cuccu, R., Elefante, S., Zinno, I., Manunta, M., Casola, V., Rivolta, G., Lanari, R. and Casu, F., 2015. An on-demand web tool for the unsupervised retrieval of earth's surface deformation from SAR data: The P-SBAS service within the ESA G-POD environment. Remote Sensing, 7(11), 15630-15650.

De Luca, C., Valerio, E., Giudicepietro, F., Macedonio, G., Casu, F. and Lanari, R., 2022. Pre-and Co-Eruptive Analysis of the September 2021 Eruption at Cumbre Vieja Volcano (La Palma, Canary Islands) Through DInSAR Measurements and Analytical Modeling. Geophysical Research Letters, 49(7), e2021GL097293. https://doi.org/10.1029/2021GL097293

Di Paola, G.M., 1972. The Ethiopian Rift Valley (between 7 00′ and 8 40′ lat. north). Bulletin Volcanologique, 36(4), 517-560.

Ebinger, C.J. and Casey, M., 2001. Continental breakup in magmatic provinces: An Ethiopian example. Geology, 29(6), 527-530.

Farr, T.G. and Kobrick, M., 2000. Shuttle Radar Topography Mission produces a wealth of data. Eos, Transactions American Geophysical Union, 81(48), 583-585. https://doi.org/10.1029/EO081i048p00583

Farr, T.G., Rosen, P.A., Caro, E., Crippen, R., Duren, R., Hensley, S., Kobrick, M., Paller, M., Rodriguez, E., Roth, L. and Seal, D., 2007. The shuttle radar topography mission. Reviews of Geophysics, 45(2). https://doi.org/10.1029/2005RG000183

Fernández, J., Tizzani, P., Manzo, M., Borgia, A., González, P.J., Martí, J., Pepe, A., Camacho, A.G., Casu, F., Berardino, P. and Prieto, J.F., 2009. Gravity-driven deformation of Tenerife measured by InSAR time series analysis. Geophysical Research Letters, 36(4).

Gola, G., Bertini, G., Bonini, M., Botteghi, S., Brogi, A., De Franco, R., Dini, A., Donato, A., Gianelli, G., Liotta, D. and Manzella, A., 2017. Data integration and conceptual modelling of the Larderello geothermal area, Italy. Energy Procedia, 125, 300-309. https://doi.org/10.1016/j.egypro.2017.08.201

Goldstein, R.M. and Werner, C.L., 1998. Radar interferogram filtering for geophysical applications. Geophysical Research Letters, 25(21), 4035-4038. https://doi.org/10.1029/1998GL900033

Gottsmann, J., Biggs, J., Lloyd, R., Biranhu, Y., & Lewi, E, 2020. Ductility and compressibility accommodate high magma flux beneath a silicic continental rift caldera: Insights from Corbetti caldera (Ethiopia). Geochemistry, Geophysics, Geosystems, 21, e2020GC008952. https://doi.org/10.1029/2020GC008952

Gouin, P., 1979. Earthquake History of Ethiopia and the Horn of Africa. IDRC, Ottawa, ON, CA.

Greenfield, T., Keir, D., Kendall, J.-M., & Ayele, A, 2019a. Low-frequency earthquakes beneath Tullu Moye volcano, Ethiopia, reveal fluid pulses from shallow magma chamber. Earth and Planetary Science Letters, 526, 115782. https://doi.org/10.1016/j.epsl.2019.115782

Greenfield, T., Keir, D., Kendall, J.-M., & Ayele, A, 2019b. Seismicity of the Bora-Tullu Moye volcanic field, 2016–2017. Geochemistry, Geophysics, Geosystems, 20, 548–570. https://doi.org/10.1029/2018GC007648

Gudjónsdóttir, S.R., Ilyinskaya, E., Hreinsdóttir, S., Bergsson, B., Pfeffer, M.A., Michalczewska, K., Aiuppa, A. and Óladóttir, A.A., 2020. Gas emissions and crustal deformation from the Krýsuvík high temperature geothermal system, Iceland. Journal of Volcanology and Geothermal Research, 391, 106350. https://doi.org/10.1016/j.jvolgeores.2018.04.007

Gudbrandsson, S., Eysteinsson, H., Mamo, T., Cervantes, C. and Gíslason, G., 2020. Geology and Conceptual Model of the Tulu Moye Geothermal Project, Oromia, Ethiopia. Proceedings World Geothermal Congress Reykjavik, Iceland, 7p.

Helgadóttir, H.M., Snaebjörnsdottir, S.O., Níelsson, S., Gunnarsdóttir, S.H., Matthíasdóttir, T., Hardarson, B.S., Einarsson, G.M. and Franzson, H., 2010. Geology and hydrothermal alteration in the reservoir of the Hellisheidi high temperature system, SW-Iceland. In Proceedings, World Geothermal Congress, Bali, Indonesia (pp.25-29). https://doi: 10.13140/2.1.1008.0648

Hutchison, W., Fusillo, R., Pyle, D.M., Mather, T.A., Blundy, J.D., Biggs, J., Yirgu, G., Cohen, B.E., Brooker, R.A., Barfod, D.N. and Calvert, A.T., 2016. A pulse of mid-Pleistocene rift volcanism in Ethiopia at the dawn of modern humans. Nature Communications, 7(1), 1-12. https://doi.org/10.1002/2016GC006395

Jónsson, S., Zebker, H., Segall, P. and Amelung, F., 2002. Fault slip distribution of the 1999 M w 7.1 Hector Mine, California, earthquake, estimated from satellite radar and GPS measurements. Bulletin of the Seismological Society of America, 92(4), 1377-1389. https://doi.org/10.1785/0120000922

Kebede, S. (2016). Country update on geothermal exploration and development in Ethiopia. In Proceedings, 6th African Rift Geothermal Conference (pp. 1-15).

Korme, T., 1999. Lithologic and structural mapping of the northeast Lake Ziway area, Ethiopian Rift, with the help of landsat tm data. SINET: Ethiopian Journal of Science, 22(2), 151-174.

Korme, T., Acocella, V. and Abebe, B., 2004. The role of pre-existing structures in the origin, propagation and architecture of faults in the Main Ethiopian Rift. Gondwana Research, 7(2), .467-479. https://doi.org/10.1016/S1342-937X(05)70798-X

Lavayssière, A., Greenfield, T., Keir, D., Ayele, A. and Kendall, J.M., 2019. Local seismicity near the actively deforming Corbetti volcano in the Main Ethiopian Rift. Journal of Volcanology and Geothermal Research, 381, 227-237. https://doi.org/10.1016/j.jvolgeores.2019.06.008

Lloyd, R., Biggs, J., Wilks, M., Nowacki, A., Kendall, J.M., Ayele, A., Lewi, E. and Eysteinsson, H., 2018. Evidence for cross rift structural controls on deformation and seismicity at a continental rift caldera. Earth and Planetary Science Letters, 487, 190-200. https://doi.org/10.1016/j.epsl.2018.01.037

Lundgren, P., Girona, T., Bato, M.G., Realmuto, V.J., Samsonov, S., Cardona, C., Franco, L., Gurrola, E. and Aivazis, M., 2020. The dynamics of large silicic systems from satellite remote sensing observations: the intriguing case of Domuyo volcano, Argentina. Scientific Reports, 10(1), 1-15. https://doi.org/10.1038/s41598-020-67982-8

Manunta, M., De Luca, C., Zinno, I., Casu, F., Manzo, M., Bonano, M., Fusco, A., Pepe, A., Onorato, G., Berardino, P. and De Martino, P., 2019. The parallel SBAS approach for Sentinel-1 interferometric wide swath deformation time-series generation: Algorithm description and products quality assessment. IEEE Transactions on Geoscience and Remote Sensing, 57(9), 6259-6281.

Okada, Y., 1985. Surface deformation due to shear and tensile faults in a half-space. Bulletin of the Seismological Society of America,75(4),1135-1154.

https://doi.org/10.1785/BSSA0750041135

Pasquarè, F. and Tibaldi, A., 2007. Structure of a sheet-laccolith system revealing the interplay between tectonic and magma stresses at Stardalur Volcano, Iceland. Journal of Volcanology and Geothermal Research, 161(1-2), 131-150. https://doi.org/10.1016/j.jvolgeores.2006.11.009

Pepe, A. and Lanari, R., 2006. On the extension of the minimum cost flow algorithm for phase unwrapping of multitemporal differential SAR interferograms. IEEE Transactions on Geoscience and Remote Sensing, 44(9), 2374-2383.

Pitcher, W.S. and Bussell, M.A., 1977. Structural control of batholithic emplacement in Peru: a review. Journal of the Geological Society, 133(3), 249-255.

Samrock, F., Grayver, A.V., Bachmann, O., Karakas, Ö. and Saar, M.O., 2021. Integrated magnetotelluric and petrological analysis of felsic magma reservoirs: Insights from Ethiopian rift volcanoes. Earth and Planetary Science Letters, 559, 116765. https://doi.org/10.1016/j.epsl.2021.116765

Samrock, F., Grayver, A.V., Eysteinsson, H. and Saar, M.O., 2018. Magnetotelluric image of transcrustal magmatic system beneath the Tulu Moye geothermal prospect in the Ethiopian Rift. Geophysical Research Letters, 45(23), 12-847. https://doi.org/10.1029/2018GL080333

Siegburg M., Bull J., Nixon C., Keir D., Gernon T., Corti G., Abebe B., Sanderson D. & Ayele A, 2020 - Quantitative constraints on faulting and fault slip-rates in the northern Main Ethiopian Rift. Tectonics, 39 (8), e2019TC006046. https://doi.org/10.1029/2019TC006046.

Sigmundsson, F., Parks, M., Hooper, A., Geirsson, H., Vogfjörd, K.S., Drouin, V., Ófeigsson, B.G., Hreinsdóttir, S., Hjaltadóttir, S., Jónsdóttir, K. and Einarsson, P., 2022. Deformation and seismicity decline before the 2021 Fagradalsfjall eruption. Nature, 609(7927), 523-528. https://doi.org/10.1038/s41586-022-05083-4

Stern R.J., Nielsen K.C., Best E., Sultan M., Arvidson R.E. & Kroner A, 1990. Orientation of the late Precambrian sutures in the Arabian–Nubian Shield. Geology 18, 1103-1106.

Tadesse, A.Z., Fontijn, K., Melaku, A.A., Gebru, E.F., Smith, V.C., Tomlinson, E., Barfod, D., Gopon, P., Bégué, F., Caricchi, L. and Laha, P., 2022. Eruption frequency and magnitude in a geothermally active continental rift: The Bora-Baricha-Tullu Moye volcanic complex, Main Ethiopian Rift. Journal of Volcanology and Geothermal Research, 423, 107471.

Teklemariam, M., Battaglia, S., Gianelli, G. and Ruggieri, G., 1996. Hydrothermal alteration in the Aluto-Langano geothermal field, Ethiopia. Geothermics, 25(6), 679-702. https://doi.org/10.1016/S0375-6505(96)00019-3

Temtime, T., Biggs, J., Lewi, E., Hamling, I., Wright, T. and Ayele, A., 2018. Spatial and temporal patterns of deformation at the Tendaho geothermal prospect, Ethiopia. Journal of Volcanology and Geothermal Research, 357, 56-67. https://doi.org/10.1016/j.jvolgeores.2018.04.004

Teng, Y. and Koike, K., 2007. Three-dimensional imaging of a geothermal system using temperature and geological models derived from a well-log dataset. Geothermics, 36(6), 518-538. https://doi.org/10.1016/j.geothermics.2007.07.006

Tibaldi, A., Vezzoli, L., Pasquaré, F.A. and Rust, D., 2008. Strike-slip fault tectonics and the emplacement of sheet–laccolith systems: the Thverfell case study (SW Iceland). Journal of Structural Geology, 30(3), 274-290. https://doi.org/10.1016/j.jsg.2007.11.008

Tolstoy, M., Waldhauser, F., Bohnenstiehl, D.R., Weekly, R.T. and Kim, W.Y., 2008. Seismic identification of along-axis hydrothermal flow on the East Pacific Rise. Nature, 451(7175), 181-184. https://doi.org/10.1038/nature06424

Tortelli, G., Gioncada, A., Pagli, C., Braschi, E., Gebru, E. F., and Keir, D., 2022. Constraints on the magma source and rift evolution from geochemistry of the Stratoid flood basalts (Afar, Ethiopia). Geochemistry, Geophysics, Geosystems, 23, e2022GC010434. http://doi.org/0.1029/2022GC010434.

United Nations Development Programme (UNDP), 1973. Geology, geochemistry and hydrology of hot springs of the East African Rift system within Ethiopia. Investigation of Geothermal Resources for Power Development (Tech. Rep. DP/SF/UN 116, 275 pp.). United Nations, New York, NY

Varet, J., Birba, E., 2018. Tulu Moye Geothermal Project (Oromia, Ethiopia). Proceedings 7th African Rift geothermal Conference Kigali, Rwanda, 14p.

Wadge, G., Biggs, J., Lloyd, R. and Kendall, J.M., 2016. Historical volcanism and the state of stress in the East African Rift System. Frontiers in Earth Science, 4, 86. https://doi.org/10.3389/feart.2016.00086

Wang, H., Elliott, J.R., Craig, T.J., Wright, T.J., Liu-Zeng, J. and Hooper, A., 2014. Normal faulting sequence in the Pumqu-Xainza Rift constrained by InSAR and teleseismic body-wave seismology. Geochemistry, Geophysics, Geosystems, 15(7), 2947-2963. https://doi.org/10.1002/2014GC005369

WoldeGabriel, G., Aronson, J.L., Walter, R.C., 1990. Geology, geochronology, and rift basin development in the central sector of the Main Ethiopia Rift. Geological Society of America Bulletin 102 (4), 439–458.

Wolfenden, E., Ebinger, C., Yirgu, G., Deino, A. and Ayalew, D., 2004. Evolution of the northern Main Ethiopian rift: birth of a triple junction. Earth and Planetary Science Letters, 224(1-2), 213-228. https://doi.org/10.1016/j.epsl.2004.04.022

Wright, T.J., Lu, Z. and Wicks, C., 2003. Source model for the Mw 6.7, 23 October 2002, Nenana mountain earthquake (Alaska) from InSAR. Geophysical Research Letters, 30(18). https://doi:10.1029/2003GL018014